CHEMISTRY OF MATERIALS

Open Access

pubs.acs.org/cm

Article

Concentration-Dependent Layer-Stacking and the Influence on Phase-Conversion in Colloidally Synthesized WSe_2 Nanocrystals

Jessica Q. Geisenhoff, Yuanhui Pan, Hang Yin, Francesco Paesani, and Alina M. Schimpf*

Cite This: *Chem. Mater.* 2024, 36, 8834−8845

Read Online

ACCESS | Metrics & More | Article Recommendations | Supporting Information

ABSTRACT: We report a synthesis of WSe_2 nanocrystals in which the number of layers is controlled by varying the precursor concentration. By altering the ratios and concentrations of $W(CO)_6$ and Ph_2Se_2 in trioctylphosphine oxide, we show that high [Se] and large Se/W ratios lead to an increased number of layers per nanocrystal. As the number of layers per nanocrystal is increased, the nanocrystal ensembles show less phase-conversion from the metastable 2M phase to the thermodynamically favored 2H phase. Density functional theory calculations indicate that the interlayer binding energy increases with the number of layers, indicating that the stronger interlayer interactions in multilayered nanocrystals may increase the energy barrier to phase-conversion. The results presented herein provide insights for directing phase-conversion in solution-phase syntheses of transition metal dichalcogenides.

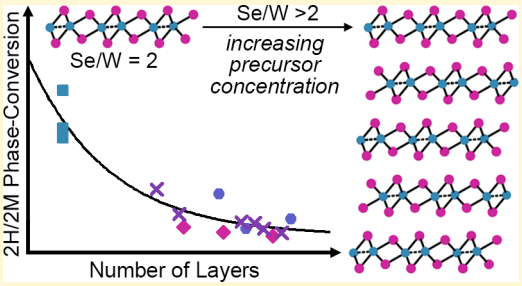

INTRODUCTION

Layered transition metal dichalcogenides (TMDs) have accrued much interest due to the unique electronic properties imparted by the two-dimensional structure.[1,2] Group-VI TMDs, including MoS_2, $MoSe_2$, WS_2, WSe_2 and $MoTe_2$, are unique in that the thermodynamically favored phase is semiconducting[3−5] with a direct bandgap at the monolayer,[6,7] making them attractive candidates for optoelectronic applications.[8−10] Furthermore, due to the lack of inversion symmetry at the monolayer, this bandgap is valley-dependent, enabling quantum control of the valley pseudospin for use in information processing.[11−14] Application of TMDs thus benefits from reliable control over the number of layers.

Group-VI TMDs have long been understood to exhibit polymorphism,[15−17] but only recently have the additional phases been fully characterized.[18−20] In these TMDs, the thermodynamically favored phase crystallizes in the hexagonal $P6_3/mmc$ space group with two layers per unit cell (thus denoted 2H) and is built from metal atoms coordinated by chalcogens in a trigonal prismatic geometry (Figure S1a).[21−23] This is the aforementioned phase that gives rise to a semiconducting band structure. Recently, a metastable phase has been synthesized in which the metal atoms are coordinated in a distorted octahedral geometry.[18−20,24−29] Monolayers of this phase are isostructural to other distorted octahedral (1T′ or T_d) layers,[30−32] but multilayers stack in the monoclinic $C2/m$ space group with two layers per unit cell (thus denoted 2M, Figure S1b).[18−20] Group-VI TMDs with the distorted octahedral coordination are attractive due to their behavior as topological insulators at the monolayer limit[33,34] and as topological superconductors in the bulk.[18,35] Indeed, bulk 2M WS_2 has the highest intrinsically superconducting transition temperature of any TMD.[18] Due to the relatively recent discovery of the 2M phase, only a few direct syntheses have been established.[18−20,24−29] Most methods rely on postsynthetic processing to access the 2M phase by conversion from the 2H phase, where metal salts or reductants are adsorbed on the surface or intercalated into the structure. These additives then need to be removed with a washing step to yield pure 2M phase.[15,16,36−50] Alternative routes have been developed with the inclusion of alkali metals during the synthesis of the TMD, but still require a postsynthetic deintercalation step to yield pure 2M phase.[18−20,50]

Colloidal synthesis has recently emerged as a promising method to directly access metastable phases.[24−29,51−68] Solution-phase crystallizations can readily access kinetically controlled reaction regimes, in which there is a lower energy barrier to the nucleation and growth of the metastable phase compared to that of the thermodynamically favored phase.[69−71] In these cases, the metastable phase can be selected for by simply stopping the reaction prior to conversion to the thermodynamically favored phase. Although the reaction pathway is often not precisely known, this phenomenon is commonly observed during the synthesis of multiphase systems and is referred to as Ostwald's rule of stages.[72−76] Indeed, nucleation and growth of the metastable phase of

Received: June 7, 2024
Revised: August 6, 2024
Accepted: August 7, 2024
Published: September 9, 2024

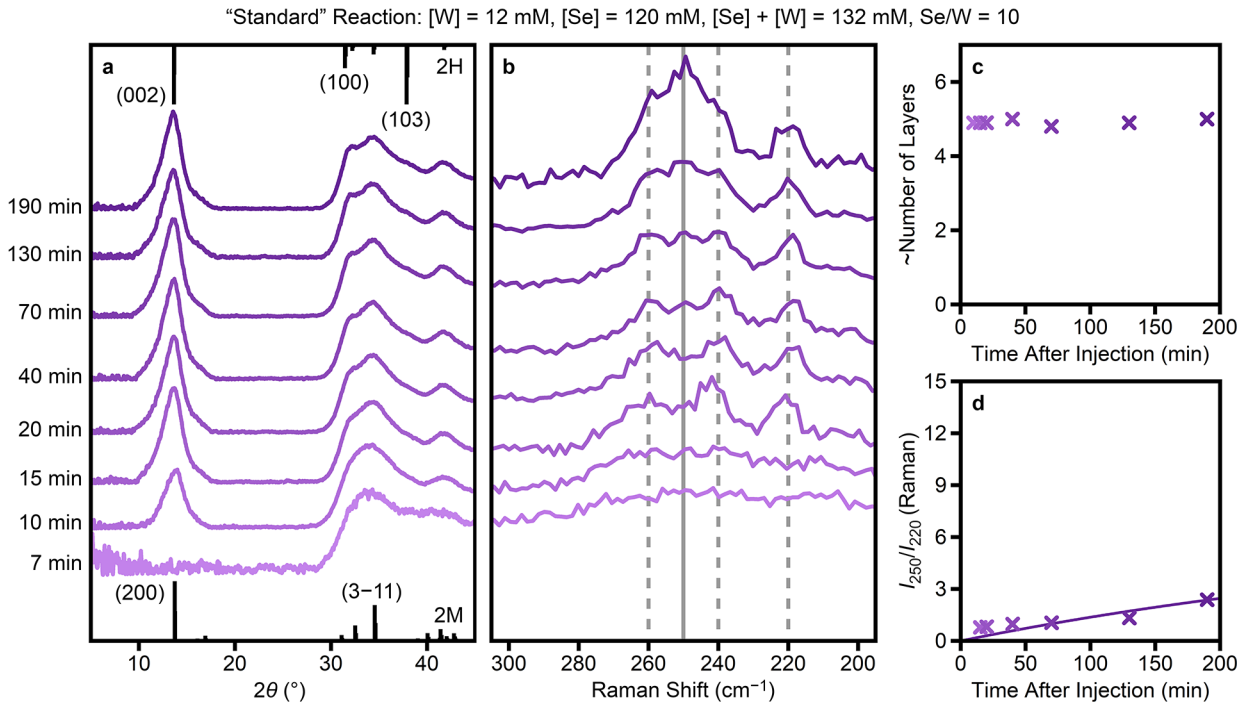

Figure 1. Characterization of WSe_2 nanocrystals synthesized with [$W(CO)_6$] = 12 mM, [Se] = 120 mM, [Se] + [W] = 132 mM, Se/W = 10. (a) Powder X-ray diffraction patterns of aliquots collected at (bottom to top) 7, 10, 15, 20, 40, 70, 130, and 190 min following injection of Ph_2Se_2. Patterns predicted from single-crystal data for the 2M (bottom)[19] and 2H (top)[22] phases of WSe_2 are shown for comparison. (b) Raman spectra of the same aliquots. Vertical lines indicate the expected peak locations for the 2M (dashed) and 2H (solid) phases. (c) Estimated number of layers and (d) ratio of the 2H (250 cm^{-1}) to 2M (220 cm^{-1}) Raman intensities as a function of time after the injection of Ph_2Se_2.

many group-VI TMDs has been observed during colloidal synthesis.[24−29,63,68,77−79]

Colloidal synthesis of WSe_2 nanocrystals serves as a useful platform for understanding factors that enable direct access to the metastable phase, in part due to the relatively small difference between the ground state energies of 2H and 2M WSe_2.[80] Many syntheses of other group-VI TMDs require charge-injection into the nanosheets from highly reducing precursors[24,28,77,81−84] or heterovalent dopants[79,85,86] to stabilize the metastable phase. The 2M phase of WSe_2, however, is readily accessed by the kinetically controlled reaction regimes achievable with colloidal synthesis.[25−29,63,68,78] For example, Sokolikova et al. demonstrated the synthesis of 2M WSe_2 at 300 °C in oleic acid using either tungsten hexachloride or tungsten hexacarbonyl ($W(CO)_6$) and trioctylphosphine selenide or elemental Se.[25] The resulting nanoflowers could then be postsynthetically converted to the 2H phase by annealing at 400 °C.[25] We have previously demonstrated a phase-selective synthesis of WSe_2 by using ligands to vary the tungsten precursor reactivity.[26] Specifically, hot-injection of Ph_2Se_2 into $W(CO)_6$ in mixtures of oleic acid (OA) and trioctylphosphine oxide (TOPO) at 330 °C resulted in more 2M phase for low TOPO/OA ratios (low reactivity), and more 2H phase for high TOPO/OA ratios (high reactivity). Importantly, this study demonstrated that the synthesesare under kinetic control by identifying the metastable 2M phase prior to conversion to the thermodynamically favored 2H phase. Although it has been clearly demonstrated that colloidal synthesis is a useful strategy in directly synthesizing the metastable phase, the crystallization pathway is still not well-understood.

Here, we present a strategy to vary the number of layers (n) and, consequently, the phase in colloidally synthesized WSe_2 nanocrystals. By adjusting the precursor ratio (Se/W) and concentrations ([Se] and [W]), we can select for nanocrystals with $n \approx 1-6$. Specifically, when Se/W = 2, primarily monolayer ($n \approx 1$) nanocrystals are formed, regardless of the precursor concentration. When Se/W > 2, multilayer ($n > 1$) nanocrystals are formed in which n depends on [Se] and [W], but is independent of Se/W. Importantly, n strongly influences the conversion of nanocrystals from the 2M to 2H phase. Monolayer nanocrystals are readily converted to the 2H phase, while multilayer nanocrystals show less phase-conversion with increasing n. We hypothesize that this decreased phase-conversion in multilayer nanocrystals is due largely to interlayer interactions, which are nonexistent in monolayer nanocrystals, allowing for facile phase-conversion. Density functional theory (DFT) calculations reveal that the interlayer binding energy increases with n, consistent with the trend of decreased phase-conversion.

RESULTS AND ANALYSIS

Figure 1 presents the characterization of our "standard" WSe_2 synthesis ([W] = 12 mM, [Se] = 120 mM, [Se] + [W] = 132 mM, Se/W = 10). Here, 21.5 mg (0.06 mmol) $W(CO)_6$ and 3.6 g TOPO were heated to 150 °C under argon and held for ~10 min to allow complete solubilization and ligand replacement of $W(CO)_6$.[63] Then, 0.31 mmol Ph_2Se_2 in 1 mL hexadecane was swiftly injected into the $W(CO)_6$ solution. Immediately following the injection, the mixture was heated to 330 °C over 10 min, after which the reaction was held for 3 h. To monitor changes in the nanocrystal morphology and phase, several aliquots were collected throughout the reaction and characterized with powder X-ray diffraction (Figure 1a) and Raman spectroscopy (Figure 1b). Details regarding the heating profile and aliquots can be found in Figure S2 and Table S1.

https://doi.org/10.1021/acs.chemmater.4c01602
Chem. Mater. 2024, 36, 8834−8845

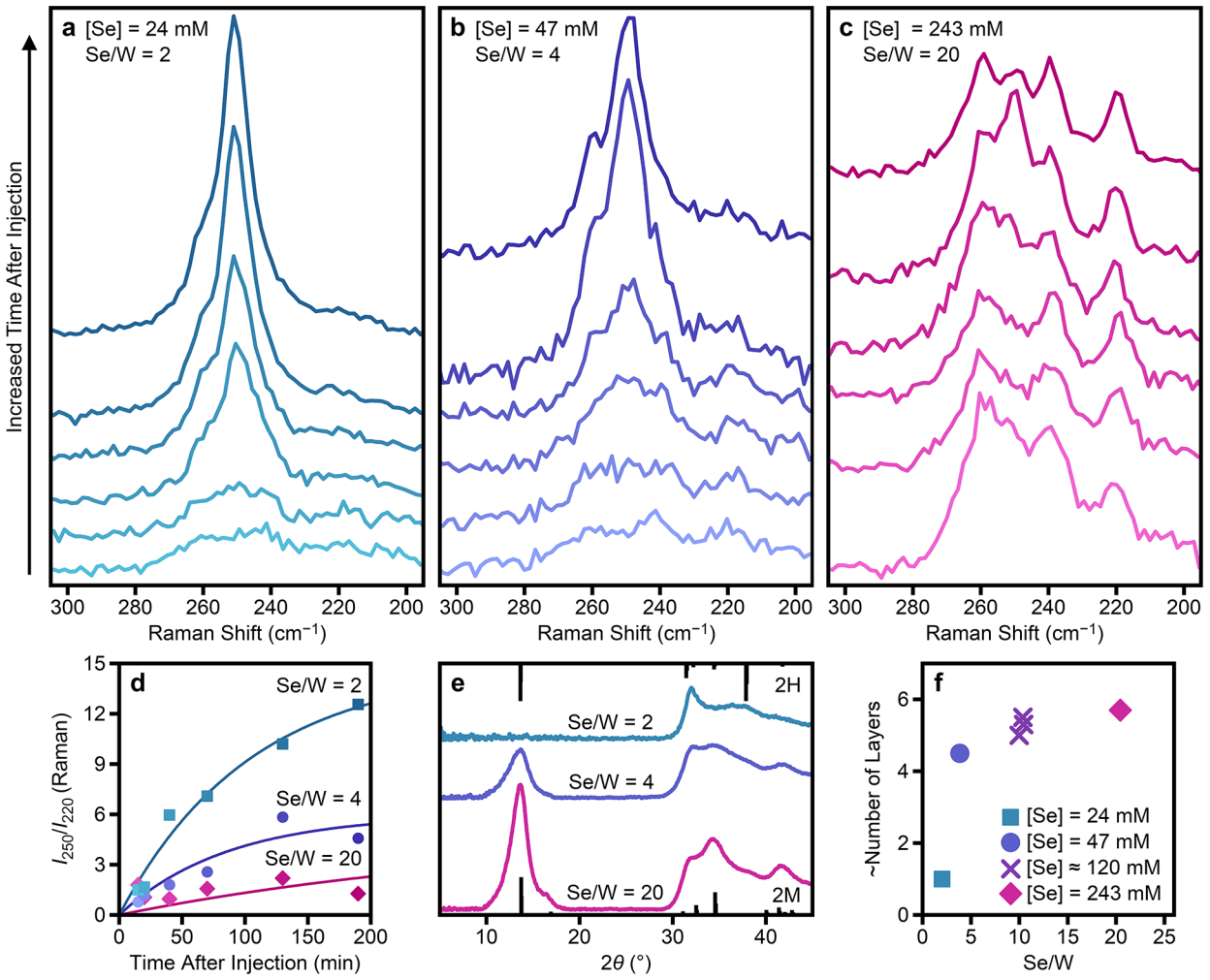

Figure 2. Raman spectra of aliquots taken during the synthesis of WSe_2 nanocrystals with [W] = 12 mM and [Se] = (a) 24 mM (2 Se/W), (b) 47 mM (4 Se/W) and (c) 243 mM (20 Se/W). (d) Ratio of the 2H (250 cm^{-1}) to 2M (220 cm^{-1}) Raman intensities as a function of time for each of the syntheses. (e) Powder X-ray diffraction patterns of the 70-min aliquots of each synthesis. Patterns predicted from single-crystal data of the 2M (bottom)[19] and 2H (top)[22] phases of WSe_2 are shown for comparison. (f) Estimated number of layers as a function of Se/W for all syntheses with [W] = 12 mM.

Powder X-ray diffraction was used primarily to monitor the nanocrystal morphology and crystallinity. Figure 1a presents the powder X-ray diffraction patterns for each aliquot collected with increasing reaction time. Patterns predicted from single-crystal data of the 2M (bottom)[19] and 2H (top)[22] phases of WSe_2 are provided for comparison. Both phases have a reflection near $2\theta \approx 13.7°$ that can be used to estimate the number of layers within the nanocrystals (the (200) reflection at $2\theta = 13.74°$ for 2M and the (002) reflection at $2\theta = 13.65°$ for 2H; herein we will refer to this as the interlayer reflection). At early time and low temperature (7 min after injection, 250 °C), there is no interlayer reflection in the powder pattern, indicating little to no stacking of monolayers. The lack of an interlayer reflection at early times could be a consequence of poor ordering in multilayered nanocrystals, but transmission electron microscopy (TEM) analysis of WSe_2 nanocrystals from similar syntheses has revealed mostly monolayer nanocrystals.[63] The broadness of this first powder pattern indicates short-range order in all directions. Once the reaction reaches 330 °C (10 min after injection), an interlayer reflection is present and other reflections become sharper, indicating an increase in crystallinity.

At 15 min, two distinct reflections begin to emerge in the region of $2\theta \approx 30–35°$. These can be assigned to the (100) reflection of the 2H phase ($2\theta \approx 32°$) and the (3−11) reflection of the 2M phase ($2\theta \approx 34°$). The (100) reflection becomes more prominent as the reaction progresses, indicating an increase in contribution from the 2H phase. Using these reflections, we can monitor the phase-conversion by defining an intensity ratio, $I_{32}/I_{34} \propto 2H/2M$. This ratio increases as the reaction progresses (Table S1), indicating conversion to the 2H phase. During this time, there is little change in the full width at half-maximum (FWHM) of the interlayer reflection, indicating negligible change in the number of layers after the first 10 min of the reaction (Figure 1c, Table S1). We note that the number of layers determined using the Scherrer equation should be considered an estimate rather than an absolute quantitative value,[87] and thus we will focus more on trends in this number rather than the specific values.

Phase identification of nanocrystalline TMDs can be challenging by powder X-ray diffraction alone due to the similarity of the 2M and 2H powder patterns and the broadness of the reflections. We thus use Raman spectroscopy as the primary tool to monitor phase-conversion. Figure 1b

https://doi.org/10.1021/acs.chemmater.4c01602
Chem. Mater. 2024, 36, 8834−8845

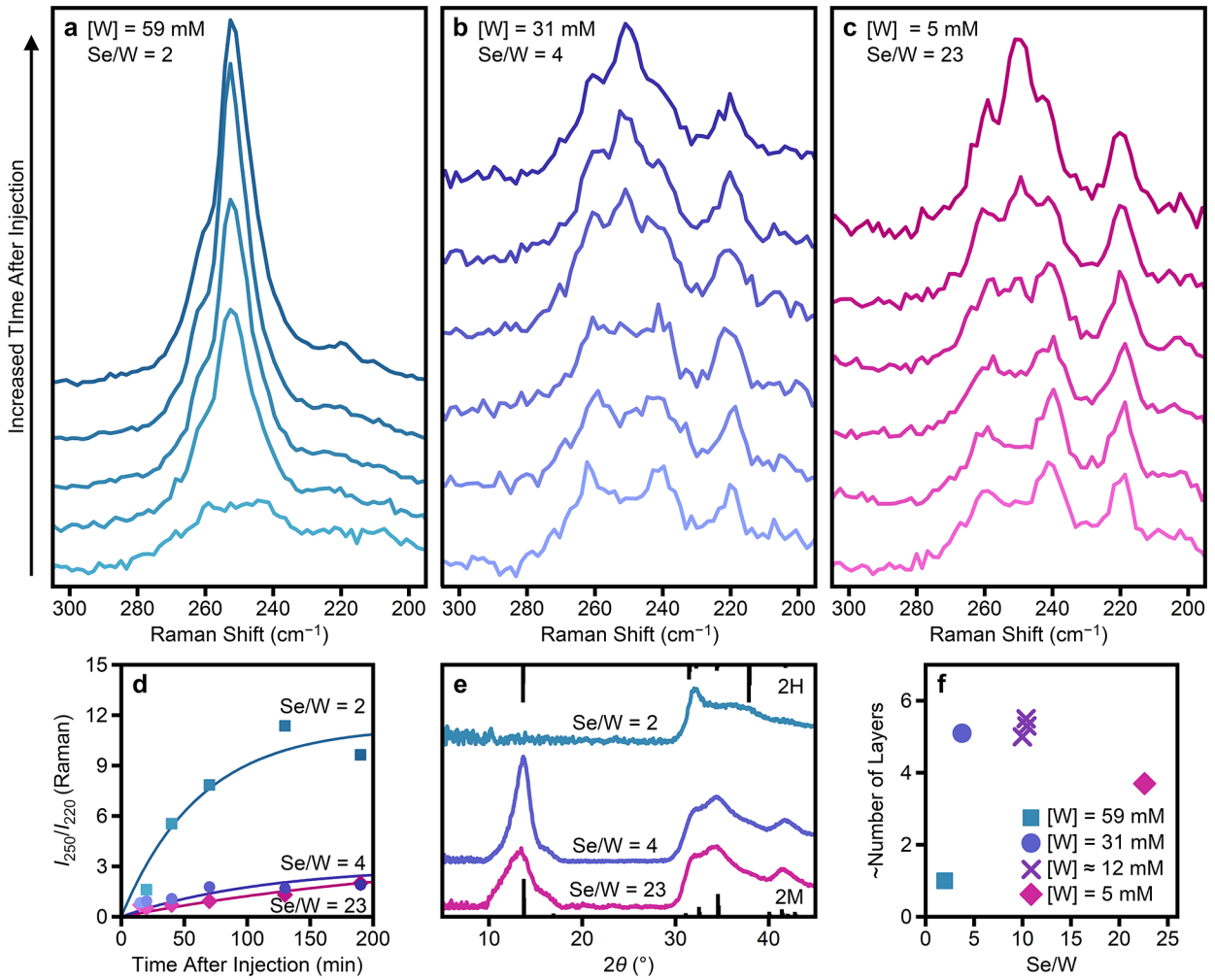

Figure 3. Raman spectra of aliquots taken during the synthesis of WSe_2 nanocrystals with [Se] ≈ 120 mM and [W] = (a) 59 mM (2 Se/W), (b) 31 mM (4 Se/W) and (c) 5 mM (23 Se/W). (d) Ratio of the 2H (250 cm^{-1}) to 2M (220 cm^{-1}) Raman intensities as a function oftime for each of the syntheses. (e) Powder X-ray diffraction patterns of the 70-min aliquots of each synthesis. Patterns predicted from single-crystal data of the 2M (bottom) and 2H (top) phases of WSe_2 are shown for comparison. (f) Estimated number of layers as a function of Se/W for all syntheses with [Se] ≈ 120 mM.

presents the Raman spectra of the same aliquots as in Figure 1a. At 5 and 10 min following the injection, no Raman modes are observed, consistent with the low crystallinity observed by X-ray diffraction. Beginning at 15 min after the injection, 3 peaks emerge near 220, 240, and 260 cm^{-1}, matching the known Raman modes of the 2M phase of WSe_2.[19,20,26] As the reaction progresses, a peak emerges at 250 cm^{-1}, matching the unresolved combination of the A_{1g} and E_{2g} modes of the 2H phase.[88−90] To track the phase-conversion, we use a ratio of the Raman intensities near 250 and 220 cm^{-1} ($I_{250}/I_{220} \propto$ 2H/2M). This ratio is plotted as a function of reaction time in Figure 1d. The solid line is a guide to the eye. We note that Raman spectroscopy is more sensitive to the 2H phase due to greater light−matter interactions of the semiconducting phase. We thus use this method to follow phase-conversion, but not to report on the quantitative phase-composition.

The reproducibility of this synthetic method was verified by performing two additional reactions with the same conditions (Figure S3, Table S2). The standard deviations of the FWHM of the (002) reflection as well as the ratio of Raman intensities (I_{250}/I_{220}) are <15% of the reported values (Table S2), suggesting that the presented method can be used to synthesize WSe_2 nanocrystals with reproducible morphology and phase. We can thus use this method to systematically evaluate the phase-conversion during the colloidal synthesis of WSe_2 nanocrystals.

The inclusion of excess chalcogen has served as a useful tool in controlling the phase[91] and morphology[92,93] of group-VI TMDs synthesized via molecular beam epitaxy and chemical vapor deposition (CVD), respectively. Analogous effects, however, have remained relatively unexplored in colloidally synthesized nanocrystals. In one study, the concentration of Mo precursor was shown to impact the size and phase of colloidally synthesized MoS_2 nanocrystals,[64] but the role of chalcogen concentration or chalcogen/metal ratio was not independently evaluated. In another example, increasing Se/W from 1 to 2 resulted in increased amounts of the 2M phase,[68] but the reason for the trend was not elucidated. Here, we synthesize a series of WSe_2 nanocrystals in which Se/W is varied first by changing [Se]. Specifically, [W] was held constant at 12 mM (matching the standard reaction), while [Se] was varied to be 24 mM (2 Se/W), 47 mM (4 Se/W) or 243 mM (20 Se/W). All other conditions were analogous to the standard reaction. The specific conditions for this series are

https://doi.org/10.1021/acs.chemmater.4c01602
Chem. Mater. 2024, 36, 8834−8845

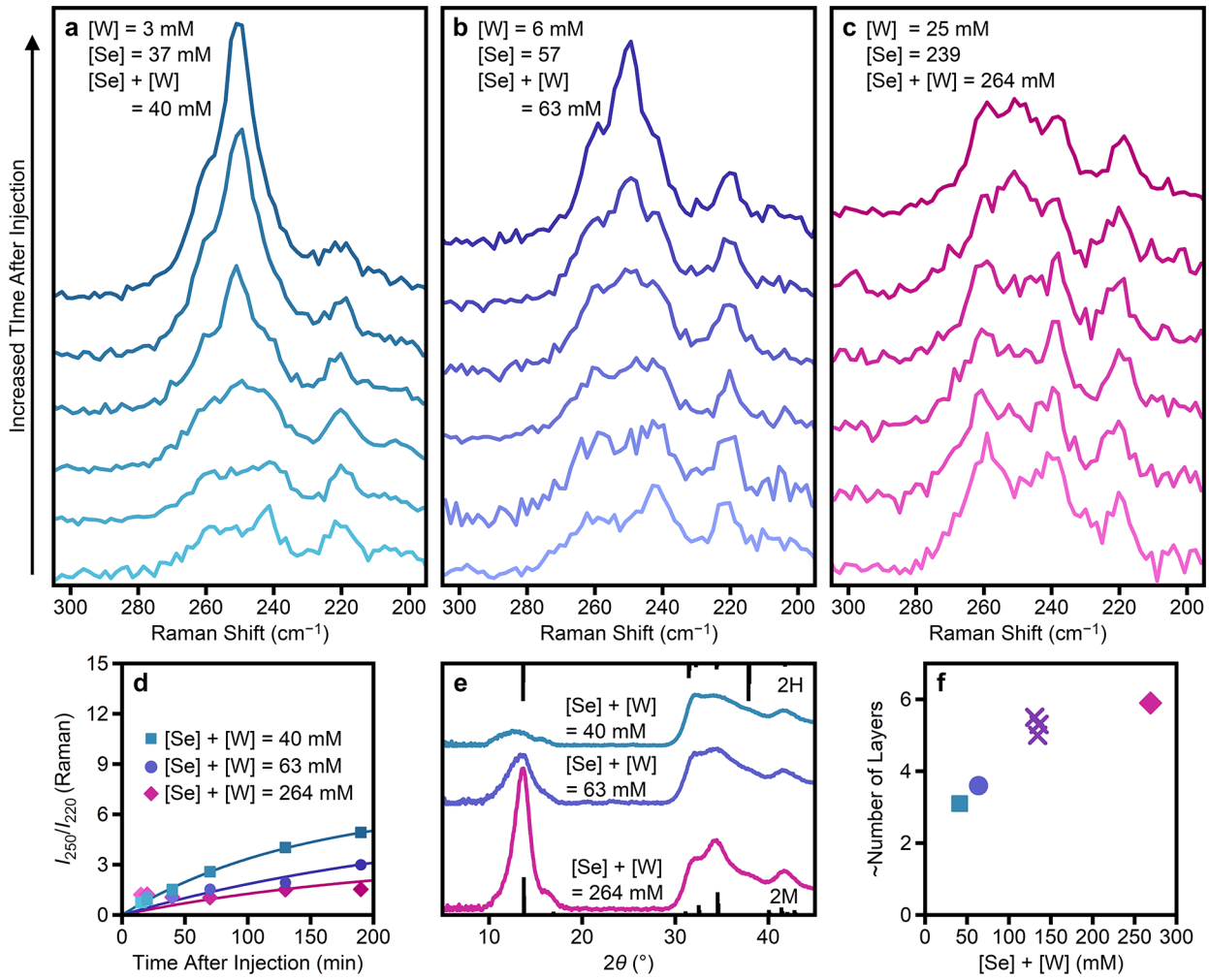

Figure 4. Raman spectra of aliquots taken during the synthesis of WSe_2 nanocrystals in which both [Se] and [W] were varied such that Se/W ≈ 10 and [Se] + [W] = (a) 40, (b) 63 and (c)264 mM. (d) Ratio of the 2H (250 cm^{-1}) to 2M (220 cm^{-1}) Raman intensities as a function of time for each of the syntheses. (e) Powder X-ray diffraction patterns of the 70-min aliquots of each synthesis. Patterns predicted from single-crystal data of the 2M (bottom) and 2H (top) phases of WSe_2 are shown for comparison. (f) Estimated number of layers as a function of Se/W for all syntheses with Se/W ≈ 10.

provided in Table S2. As described above, phase-conversion was monitored by collecting Raman spectra on aliquots with increasing reaction time (Figure 2a–c). With 2 Se/W ([Se] = 24 mM, Figure 2a), once the WSe_2 is crystalline enough to observe distinct Raman modes (aliquot 3), the spectrum consists primarily of a peak at 250 cm^{-1}. This peak is indicative of the 2H phase, which dominates the Raman spectra throughout the remainder of the reaction. As Se/W is increased to 4 ([Se] = 47 mM, Figure 2b), small contributions to the Raman spectra from peaks at 220 and 260 cm^{-1} are observed, indicative of some 2M phase. These 2M peaks, along with one at 240 cm^{-1}, are obvious at Se/W = 10 ([Se] = 120 mM, Figure 1b) and are the most prominent at Se/W = 20 ([Se] = 243 mM, Figure 2c). The effect on phase-conversion of varying Se/W by changing [Se] is summarized in Figure 2d, which shows the ratio of the Raman intensities as a function of time. The solid lines are guides to the eye. These data reveal that, as Se/W (or [Se]) increases, the extent of phase-conversion decreases. This trend is summarized in Figure S4a–d, which plots the ratios of the Raman intensities as a function of [W], [Se], [Se] + [W] and Se/W.

The powder X-ray diffraction patterns of aliquots taken earlier in the reaction (Figure 2e) reveal the same trend in phase as the Raman spectra. For the nanocrystals synthesized with 2 Se/W ([Se] = 24 mM), the (013) reflection (2θ = 37.86°) is more intense than in the other powder patterns, suggesting this nanocrystal ensemble has the most 2H phase of the series. Conversely, for nanocrystals synthesized with 20 Se/W ([Se] = 243 mM), the (−113) reflection (2θ = 34.55°) is more intense than in the other powder patterns, suggesting this nanocrystal ensemble has the most 2M phase of the series. This trend is summarized in Figure S5a–d, which plots the ratio of X-ray diffraction intensities (I_{32}/I_{34} ∝ 2H/2M) as a function of [W], [Se], [Se] + [W] and Se/W.

Interestingly, the powder patterns also reveal a change in the interlayer reflection (2θ = 13.7°) as Se/W is increased. This reflection is not observable for 2 Se/W ([Se] = 24 mM,), but appears and narrows as Se/W increases (Table S2). This observation indicates that nanocrystals synthesized at higher Se/W (or [Se]) are more stacked (i.e., have more layers). Figures 2f and S6a–d show the approximate number of layers in the nanocrystals, estimated via Scherrer analysis, as a function of [W], [Se], [Se] + [W] and Se/W. The trend

https://doi.org/10.1021/acs.chemmater.4c01602
Chem. Mater. 2024, 36, 8834−8845

observed by X-ray diffraction is corroborated by TEM, which reveals that increased Se/W (or [Se]) leads to increased stacking but does not significantly affect the lateral size of the nanocrystals (Figure S7). We note that, although the lack of an interlayer reflection in the powder pattern suggests that nanocrystals synthesized with 2 Se/W ([Se] = 24 mM) are single-layer, some multilayered nanocrystals are still observed in the TEM images. Although Scherrer analysis may provide an underestimate of sizes compared to TEM, the latter provides only a localized representation of the nanocrystal ensemble. We thus chose to use the number of layers estimated by powder X-ray diffraction to represent the trends in these experiments.

The data presented in Figure 2 suggest that increased Se yields less phase-conversion and more layers per nanocrystal. These experiments alone, however, do not distinguish between the influence of Se/W or absolute [Se]. To separate these effects, we next changed Se/W by changing [W] while keeping [Se] constant (Figure 3). For this series, [Se] was held at ∼120 mM (close to the standard reaction), while [W] was varied to be 59 mM (2 Se/W), 31 mM (4 Se/W) or 5 mM (23 Se/W). All other conditions were analogous to the standard reaction. The conditions for this series are provided in Table S2. With 2 Se/W ([W] = 59 mM, Figure 3a), once the WSe_2 is crystalline enough to observe distinct Raman modes (aliquot 2), the spectrum consists primarily of a peak at 250 cm^{-1}. This peak is indicative of the 2H phase, which dominates the Raman spectra throughout the remainder of the reaction. When Se/W is increased to 4 ([W] = 31 mM, Figure 3b), 10 ([W] = 12 mM, Figure 1b), or 23 ([W] = 5 mM, Figure 3c), distinct contributions from peaks at 220, 240 and 260 cm^{-1} are observed, indicative of some 2M phase. Interestingly, the Raman spectra reveal very little influence on phase-conversion, except at Se/W = 2 (Figures 3d, S4e−h). This trend is also observed in the powder X-ray diffraction patterns (Figures 3e, S5e−h). The large increase in phase-conversion at Se/W = 2 may suggest that nanocrystals that are primarily monolayer undergo significantly greater phase-conversion than multilayered nanocrystals (*vide infra*). Importantly, the lack of difference in phase-conversion for Se/W = 4, 10, and 23 suggests that Se/W is not the determining factor for phase-conversion and that absolute concentration ([Se] and/or [Se] + [W]) may be more important.

Figures 3f and S6e−h show the estimated number of layers as a function of [W], [Se], [Se] + [W] and Se/W. Although the number of layers drastically increases from Se/W = 2 to Se/W = 4, subsequent increases in Se/W lead to a decrease in the number of layers. These results suggest that (1) reactions with Se/W = 2 may behave differently than those with Se/W > 2 (*vide infra*) and (2) Se/W is not the determining factor in the number of layers, as the trend observed for increasing Se/W by decreasing [W] is opposite that of increasing Se/W by increasing [Se]. Taking these two series together, the data suggest that the number of layers depends on concentration rather than Se/W. Specifically, we see that decreasing [W], and therefore decreasing the overall concentration ([Se] + [W]), leads to a decrease in the number of layers (excluding Se/W = 2). Similarly, increasing [Se] (and therefore increasing [Se] + [W]), leads to an increase in the number of layers.

To confirm the influence of total concentration, a series of WSe_2 nanocrystals were synthesized in which [Se] and [W] were simultaneously adjusted to vary the total concentration ([Se] + [W]) to be 40, 63, or 264 mM while maintaining Se/W ≈ 10 to match the standard reaction. The conditions for this series are provided in Table S2. Raman spectroscopy reveals a modest decrease in phase -conversion with increasing concentration (Figures 4a−d, S4i−l) that is corroborated by power X-ray diffraction (Figures 4e, S5i−l). Taken together, these series suggest that the precursor concentration, which is dominated by [Se], is an important factor in the phase-conversion (Figures S4, S5). To corroborate this conclusion, additional reactions were performed in which [Se] and [W] were simultaneously varied to keep [Se] + [W] nearly constant while greatly varying Se/W (Figure S8, Table S2). In these reactions, a small increase in the precursor concentration results in a very small decrease in the phase-conversion (except at Se/W = 2), even with a large increase in Se/W (Figures S8d, S4m−p, S5m−p, Table S2).

Analysis of the powder X-ray diffraction patterns for nanocrystals synthesized with varying total concentration (Figure 4e) reveals that the precursor concentration also plays an important role in the number of layers per nanocrystal. Specifically, as the overall concentration is increased, so are the number of layers (Figure 4f), consistent with the results presented in the first two series (Figure S6). Additional reactions in which [Se] + [W] is kept relatively constant (Figure S8, Table S2) show a very small decrease in the number of layers with a small increase in the total concentration (except at Se/W = 2), even with a large increase in Se/W (Figures S8f, S6m−p).

DISCUSSION

Influence of Concentration on Layer Stacking. Powder X-ray diffraction of aliquots from the standard reaction (Figure 1a) indicates that WSe_2 nanocrystals synthesized herein nucleate primarily as monolayers, as evidenced by the lack of an interlayer reflection 7 min after Ph_2Se_2 injection. Once the reaction reaches 330 °C (10 min after Ph_2Se_2 injection), the nanocrystals have reached a final size (∼5 layers in the standard reaction).

The number of layers per nanocrystal is influenced by both precursor ratio (Se/W) and concentration. This effect can be divided into two regimes: Se/W = 2 and Se/W > 2. For the syntheses presented herein, all reactions with Se/W = 2 resulted in primarily monolayer nanocrystals (Figure S9). For Se/W > 2, the number of layers per nanocrystal has no obvious dependence on Se/W and increases moderately as the precursor concentration increases (Figure S9). The presence of two different growth regimes depending on chalcogen/metal ratio has also been reported in CVD-synthesized MoS_2, where lower S/Mo ratios led to primarily heterogeneous growth and monolayer crystals, while higher S/Mo introduced significant homogeneous nucleation and interlayer growth.[92] Similarly, in CVD-synthesized WS_2/WSe_2 lateral heterostructures, low Se/W led to only monolayer WSe_2 growth, while high Se/W was used to grow WSe_2 bilayers.[93] This selectivity was attributed to differences in the adsorption and diffusion behaviors of reactive clusters present at different Se/W ratios, where a significant amount of WSe_3 clusters was needed to form bilayer WSe_2, while WSe and WSe_2 clusters would form only monolayer WSe_2. Additionally, inclusion of excess chalcogen in hydrothermally synthesized $MoSe_2$ has been reported to lead to interstitial Se that bridges layers through Se−Se bonding.[94,95] The ability of Se atoms to add to the basal plane may further facilitate interlayer growth at higher Se/W and [Se]. Finally, the near-absence of interlayer growth for Se/W = 2 may also

https://doi.org/10.1021/acs.chemmater.4c01602
Chem. Mater. 2024, 36, 8834−8845

be due to the presence of Se vacancies at low Se/W. Computational analysis indicates that Se vacancies weaken the interlayer interactions (Figure S10, Table S3), potentially leading to decreased layer assembly.

Influence of Concentration on Phase-Conversion. The presence of the metastable 2M phase at early times, followed by conversion to the thermodynamically favored 2H phase, suggests that the reactions herein are under kinetic control. Nucleation in the metastable phase followed by conversion to the thermodynamically favored phase is consistent with Ostwald's rule,[72] which has been validated in colloidal syntheses of CdSe nanocrystals.[96,97] Such kinetically controlled growth has been observed for many syntheses of WSe_2 nanocrystals[25−27,63,78] and is likely enabled due to the relatively low temperatures used in nanocrystal syntheses compared to other synthetic methods. Nucleation in the 2M phase, combined with the rapid reactivity of the precursors in TOPO,[63] likely enables phase-conversion of already nucleated nanocrystals rather than separate nucleation of the 2H phase.

Similar to the layer stacking, the phase-conversion is influenced by both precursor ratio (Se/W) and concentration and can again be divided into the regimes of Se/W = 2 and Se/W > 2. For reactions with Se/W > 2, the phase-conversion has no obvious dependence on Se/W and is inversely proportional to the precursor concentration (Figures S11, S12), with higher concentrations leading to less phase-conversion. This trend does not hold for reactions with Se/W = 2, which all have similar phase-conversion that is greater than all reactions with Se/W > 2 (Figures S11, S12). It is worth noting that these reactions also result in primarily monolayer nanocrystals, suggesting that the number of layers may play a role in phase-conversion (*vide infra*). Additionally, Se vacancies at low Se/W may further promote phase-conversion, as defects are expected to facilitate structural relaxation.[97]

Phase-Conversion Pathway and Dependence on the Number of Layers. For the synthesis presented herein, the two available phase-conversion mechanisms[98] are solution-mediated (Figure 5, top)[99] or solid-state (Figure 5, bottom).[100] In the former, 2M nanocrystals would dissolve and recrystallize in the 2H phase. In the latter, the 2H phase would nucleate within the 2M nanocrystals to begin the phase-transition process. Given that higher precursor concentrations are expected to hinder dissolution of nucleated nanocrystals, a dependence of phase-conversion on precursor concentration is expected for a dissolution and recrystallization mechanism. Additionally, increased phase-conversion with smaller size (fewer layers) is expected for a solution-mediated phase-conversion.[99] Upon closer inspection, however, two observations suggest that a solid-state phase-transformation may also contribute. First, as discussed above, nanocrystals with high precursor concentration but only 2 Se/W show the greatest amount of phase-conversion, suggesting that concentration is not the dominating influence on phase-conversion. Second, when nanocrystals were nucleated at higher concentrations and subsequently diluted for growth, no evidence of dissolution was observed (Figures S13, S14). As both the number of layers and the phase-conversion are concentration-dependent, dilution during growth would be expected to cause a broadening of the interlayer reflections and an increase in phase-conversion if the nanocrystals were dissolving and recrystallizing. In contrast, there is no significant change in the number of layers per nanocrystal upon dilution (Figures S13b, S14b; Table S4), and the final phase matches that of the undiluted reaction (Figures S13c, S14c; Table S4). These results suggest that the concentrations at nucleation (rather than during growth) are determining the final nanocrystal phase and morphology, indicating limited dissolution and recrystallization.

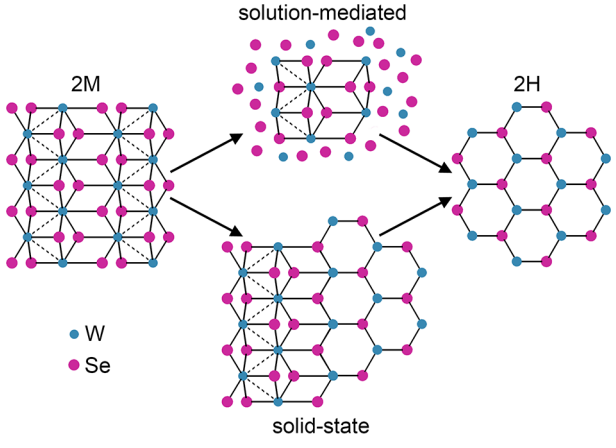

Figure 5. Schematic representation of possible phase-conversion pathways.

Based on the observations above, we hypothesize that precursor concentration and ratio play primarily an indirect role in the phase-conversion by influencing the number of layers, which, in turn, heavily influences the phase-conversion. Previous DFT calculations on 2H MoS_2 have found an increase in the interlayer binding energy (IBE) with increasing number of layers[101] and our calculations reveal the same trend for 2M WSe_2 (Figure 6a). The IBE increases sharply up to 4 layers, after which it plateaus. This increase in IBE is expected to hinder atom diffusion, decreasing the phase-conversion for nanocrystals with more layers. To summarize this influence, the phase-conversion (as determined by Raman spectroscopy, $I_{250}/I_{220} \propto$ 2H/2M) is plotted as a function of the estimated number of layers per nanocrystal in Figure 6b. For primarily monolayer nanocrystals, the lack of IBE is expected to allow for facile atom diffusion and phase-conversion, consistent with the high 2H/2M ratio for these ensembles. In nanocrystals with >4 layers, there is negligible decrease in the phase-conversion with increasing number of layers. These ensembles also show a very mild dependence on Se/W, with greater Se excess leading to less phase-conversion. This trend could be due to interstitial bridging Se,[68,94,95] which would be expected to hinder atom diffusion.

Contributions from solution-mediated phase-conversion could complement solid-state phase-conversion, for example, by enabling surface nucleation of the 2H phase, which then propagates through the nanocrystal. We hypothesize that phase-conversion initiated by internal defects is minimal, as such a mechanism would be expected to have increased phase-conversion for larger (more layers) nanocrystals.[100] We note that for μm-scale, mechanically exfoliated 2M WS_2, monolayers were reported to be more stable against phase-conversion than multilayers.[102] This trend, however, was primarily attributed to higher thermal conductivity and greater heat dissipation, which are not expected to be dominant factors in colloidal nanocrystals.

https://doi.org/10.1021/acs.chemmater.4c01602
Chem. Mater. 2024, 36, 8834−8845

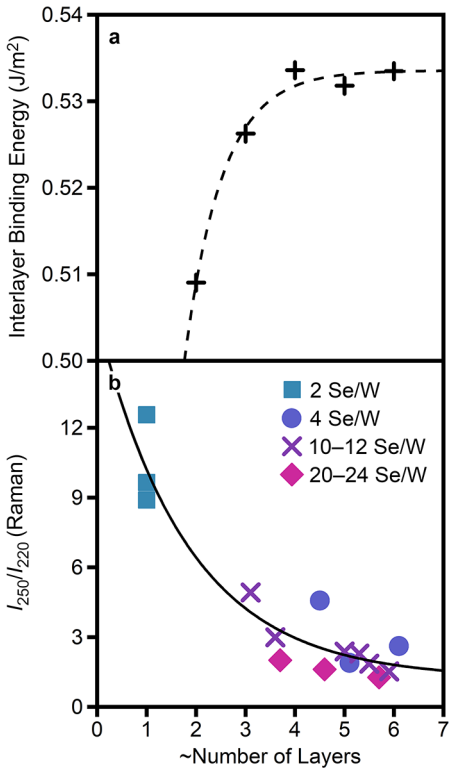

Figure 6. (a) Interlayer binding energies and (b) ratio of Raman intensities corresponding to the 2H and 2M phases (taken near 250 and 220 cm^{-1}, respectively) plotted as a function of the estimaed number of layers per nanocrystal. The dashed and solid lines are guides to the eye.

SUMMARY AND CONCLUSIONS

We have investigated the role of precursor concentration and ratio in dictating the layer-stacking and phase-conversion in colloidally synthesized WSe_2 nanocrystals. Importantly, the effect of concentration and ratio were deconvoluted by performing several series of reactions in which Se/W was varied by changing [Se] or [W], or was kept constant while changing both [Se] and [W]. Under these conditions, Se/W = 2 yields primarily monolayer nanocrystals, while Se/W > 2 yields multilayer nanocrystals in which the number of layers is independent of Se/W and increases modestly with increasing precursor concentration. These synthetic investigations revealed an inverse correlation between the phaseconversion and the number of layers. We hypothesize that this trend is due to increased interlayer interactions in multilayer nanocrystals that inhibit phase-conversion. In contrast, monolayer nanocrystals undergo nearly complete phase-conversion, even at high precursor concentrations, suggesting that dissolution is not a limiting factor. Overall, these studies provide insight into the factors that can be used tailor layer-stacking and/or phase in colloidally synthesized TMD nanocrystals.

EXPERIMENTAL METHODS

Chemicals. A list of chemicals, purities and manufacturers is provided in Table S5. All chemicals were used without further purification. TOPO, hexadecane, $W(CO)_6$ and Ph_2Se_2 were stored in a nitrogen-filled glovebox. Toluene and methanol (MeOH) were stored under ambient conditions.

Synthesis. *Synthesis of WSe_2 Nanocrystals under the Standard Conditions.* Glassware and stir bars were dried in an oven at 120 °C. In a nitrogen-filled glovebox, a 4-neck, 25-mL, round-bottom flask was loaded with a glass-coated stir bar, 21.5 mg (0.0611 mmol) $W(CO)_6$ and 3.6 g TOPO (4.1 mL, 9.3 mmol). The flask was fitted with two ceramic sheaths (through rubber septa), a condenser with a flow/hose-adapter and a septum. Separately, a 3-neck, 25-mL, round-bottom flask was loaded with a glass-coated stir bar, 190.5 mg (0.6104 mmol) Ph_2Se_2 and 1.546 g (2 mL, 6.828 mmol) hexadecane. The flask was fitted with two septa and a flow adapter. Both flasks were removed from the glovebox and placed on the Schlenk line. The space between the flow adapters and the Schlenk line was evacuated (5−10 min) and refilled with argon three times. The flasks were then opened to the line and evacuated (~20 min) and refilled with argon three times. After the final refilling of argon, the flask containing $W(CO)_6$ was heated to 150 °C using a proportional−integral−derivative (PID) controller and held for 10 min. At ~70 °C, the solution turned yellow and gas-evolution was observed. Meanwhile, the flask containing Ph_2Se_2 was heated to 70 °C to ensure complete dissolution of the Ph_2Se_2 and avoid large temperature drops after the injection. After both solutions are appropriately heated, 1.0 mL Ph_2Se_2 solution (0.31 mmol Ph_2Se_2) was injected into the $W(CO)_6$ solution. Immediately after the injection, the solution was heated to 330 °C using a PID controller with a preprogrammed heating profile (Figure S2). During this heating, rapid gas-evolution was observed and the solution became brown/black. Aliquots were taken from the reaction by removing ~0.1 mL using a purged 1-mL syringe and needle. Aliquots were immediately injected into a vial containing 1 mL toluene to prevent solidification of the TOPO. The reaction was held for a total of 190 min (starting from the Ph_2Se_2 injection), after which it was cooled by removal of the heating mantle. When the reaction mixture reached ~80 °C, septa were removed from the flask and ~5 mL toluene was added to avoid solidification. Aliquots and final reaction solutions were transferred to centrifuge tubes (each aliquot was split into 2 tubes) and MeOH was added in a 2:1 volume ratio. The slurries were centrifuged for 5 min at 8000 rpm. The nanocrystals were washed two additional times by redispersing in toluene, adding MeOH (2:1 MeOH:toluene by volume), and centrifuging for 5 min at 8000 rpm. Following the final wash, 0.5 mL toluene was added to one tube to prepare a stock solution to use for characterization by TEM and Raman. The sample in the other tube was dried and used for powder X-ray diffraction measurements.

Synthesis of WSe_2 Nanocrystals with Varying Precursor Concentrations and Ratios. Nanocrystals were synthesized in the manner described above using the same amount of TOPO. The amounts of $W(CO)_6$ and/or Ph_2Se_2 were varied to obtain the conditions specified in Table S2.

Dilution of Nanocrystals following Nucleation at Higher Concentration. In the first reaction (Figure S13), WSe_2 nanocrystals were synthesized as described above using 40.1 mg (0.114 mmol) $W(CO)_6$, 401.0 mg (1.285 mmol) Ph_2Se_2, and 3.6280 g (4.123 mL, 9.383 mmol) TOPO. At 15 min following injection, 0.7 mL was removed from the reaction and injected into a separate 25-mL, 4-neck round-bottom flask containing 3.1666 g (3.598 mL, 8.190 mmol) TOPO heated to 330 °C. The reaction was held at this temperature and 0.3 mL aliquots were taken over the course of 4 h to monitor morphology- and phase-changes. In the second reaction (Figure S14), WSe_2 nanocrystals were synthesized as described above using 19.9 mg (0.0566 mmol) $W(CO)_6$, 190.9 mg (0.610 mmol) Ph_2Se_2, and 3.6105 g (3.1772 mL, 9.338 mmol) TOPO. At 15 min following injection, 0.7 mL was removed from the reaction and injected into a separate 25-mL, 4-neck round-bottom flask containing 3.1666 g (3.598 mL, 8.190 mmol) TOPO heated to 330 °C. The reaction was held at this temperature and 0.3 mL aliquots were taken over the course of 24 h to monitor morphology and phase-changes.

Characterization. *Raman Spectroscopy.* Samples were prepared and analyzed under ambient conditions. The stock solution of nanocrystals suspended in toluene was drop-cast onto a polished silicon substrate (Silicon Valley Microelectronics). Raman spectra were collected using a Renishaw inVia confocal Raman microscope with 532-nm laser-excitation (10 mW) and a 50× objective lens. To process the data, a linear background was fit between 180 and 301

https://doi.org/10.1021/acs.chemmater.4c01602
Chem. Mater. 2024, 36, 8834−8845

cm^{-1} and subtracted from the spectra. I_{250}/I_{220} was taken as the ratio of the maximum intensities near 250 and 220 cm^{-1}.

Powder X-ray Diffraction. Samples were prepared and analyzed under ambient conditions. After washing the nanocrystals, excess solvent was removed under vacuum, leaving a pellet of nanocrystals (~20 mg). Dried samples were transferred to a loop using paraffin oil. Powder X-ray diffraction patterns were collected using a D8 Smart diffractometer with a Pt 135 detector equipped with a Rigaku MicroMax-007HF High-Intensity Microfocus rotating anode with Cu Kα radiation (λ = 1.54184 Å) at 40 kV, 30 mA and Varimax-HF double bounce optics. Diffraction images were merged/integrated in Diffrac.EVA V.4.3.0.1(Bruker) with background removal using a curvature of 0.06 and a threshold of 1.000. I_{32}/I_{34} was taken as the ratio of intensities at 2θ = 31.98 and 34.32°. When an interlayer reflection was present, the number of layers was estimated using the Scherrer equation with κ = 0.9 assuming a lattice constant of a = 13.8 Å for 2M WSe_2. Using the interlayer lattice constant for 2H WSe_2 (c = 12.96 Å) would result in a slightly greater number of layers ($n_{2H} = 1.06n_{2M}$), but this difference is not significant for the analysis presented herein. The FWHM of the interlayer reflection was determined by taking the difference in 2θ between the two points at which the intensity was half the maximum intensity of the peak.

Transmission Electron Microscopy. TEM grids were prepared by drop-casting a single drop of stock-solution onto a 100-mesh copper grid coated with Formvar and carbon (Electron Microscopy Sciences). Images were collected on a ThermoFischer Talos F200X G2 operating at 200 keV. Lateral sizes were measured in ImageJ. For nanocrystals with the stacking direction parallel to the grid ("top" view), the lateral size was measured as the longest distance across the nanocrystal. For nanocrystals with the stacking direction parallel to the grid ("side" view), the lateral size was measured as the length of the longest layer. The number of layers was determined via manual counting of the layers in each nanocrystal oriented with the stacking direction parallel to the TEM grid ("side" view).

Computations. DFT calculations were performed using the Vienna *Ab initio* Simulation Package (VASP)[103] to determine the IBEs of 2M WSe_2. The IBEs with or without vacancies were calculated as described previously for MoS_2.[101] In all DFT calculations, the Perdew–Burke–Ernzerhof (PBE)[104] exchange-correlation functional was employed.[105,106] The core electrons were described using the projector augmented wave (PAW) method.[107] A plane-wave basis set with an energy cutoff of 500 eV was used in all calculations. The convergence criteria for the energies and forces were set to 1×10^{-4} eV and 0.001 eV $Å^{-1}$, respectively. Along the stacking direction, a vacuum space of more than 20 Å was applied in all few-layered systems to avoid spurious interactions between the periodic images. To better describe van der Waals interactions, the empirical correction developed by Grimme was adopted in combination with the Becke-Johnson damping function (D3(BJ)).[108−110] After structural relaxation, Γ-centered k-point meshes with a resolution of 0.25 $Å^{-1}$ were chosen to calculate the total energies necessary to determine the IBEs.

■ ASSOCIATED CONTENT

Supporting Information

The Supporting Information is available free of charge at https://pubs.acs.org/doi/10.1021/acs.chemmater.4c01602.

Additional characterization, tabulation of synthesis parameters, phase analysis, and additional DFT calculations (PDF)

■ AUTHOR INFORMATION

Corresponding Author

Alina M. Schimpf − *Department of Chemistry and Biochemistry, University of California, San Diego, La Jolla, California 92093, United States; Program in Materials Science and Engineering, University of California, San Diego, La Jolla, California 92093, United States;* orcid.org/0000-0001-5402-7426; Email: aschimpf@ucsd.edu

Authors

Jessica Q. Geisenhoff − *Department of Chemistry and Biochemistry, University of California, San Diego, La Jolla, California 92093, United States*

Yuanhui Pan − *Department of Chemistry and Biochemistry, University of California, San Diego, La Jolla, California 92093, United States;* orcid.org/0000-0002-2304-6314

Hang Yin − *Department of Chemistry and Biochemistry, University of California, San Diego, La Jolla, California 92093, United States*

Francesco Paesani − *Department of Chemistry and Biochemistry, University of California, San Diego, La Jolla, California 92093, United States; Program in Materials Science and Engineering, University of California, San Diego, La Jolla, California 92093, United States;* orcid.org/0000-0002-4451-1203

Complete contact information is available at: https://pubs.acs.org/10.1021/acs.chemmater.4c01602

Notes

The authors declare no competing financial interest.

■ ACKNOWLEDGMENTS

This research was supported by the U.S. National Science Foundation (CHE-2003675 to A.M.S.). Raman spectroscopy was performed using facilities supported by the NSF through the UC San Diego Materials Research Science and Engineering Center (UCSD MRSEC, DMR-2011924). TEM images were collected at the San Diego Nanotechnology Infrastructure (SDNI) of UCSD, a member of the National Nanotechnology Coordinated Infrastructure, which is supported by the National Science Foundation (ECCS-2025752). Powder X-ray diffraction measurements were performed at the UC San Diego Crystallography Facility. Y.P. and F.P. were supported by the Department of Energy, Basic Energy Science (BES) Office through award no. DE-SC0022332. Computational resources were provided by the National Energy Research Scientific Computing Center (NERSC), supported by Department of Energy BES Office under contract DE-AC02-05CH11231 and the Triton Shared Computing Cluster (TSCC) at the San Diego Supercomputer Center (SDSC).

■ REFERENCES

(1) Liu, G. B.; Xiao, D.; Yao, Y. G.; Xu, X. D.; Yao, W. Electronic Structures and Theoretical Modelling of Two-Dimensional Group-VIB Transition Metal Dichalcogenides. *Chem. Soc. Rev.* **2015**, *44*, 2643.

(2) Lebègue, S.; Eriksson, O. Electronic Structure of Two-Dimensional Crystals from Ab Initio Theory. *Phys. Rev. B* **2009**, *79*, No. 115409.

(3) Manzeli, S.; Ovchinnikov, D.; Pasquier, D.; Yazyev, O. V.; Kis, A. 2D Transition Metal Dichalcogenides. *Nat. Rev. Mater.* **2017**, *2*, No. 17033.

(4) Goodenough, J. B. Band Model for Transition-Metal Chalcogenides Having Layer Structures with Occupied Trigonal-Bipyramidal Sites. *Mater. Res. Bull.* **1968**, *3*, 409.

(5) Huisman, R.; Dejonge, R.; Haas, C.; Jellinek, F. Trigonal-Prismatic Coordination in Solid Compounds of Transition Metals. *J. Solid State Chem.* **1971**, *3*, 56.

(6) Sun, Y. J.; Wang, D.; Shuai, Z. G. Indirect-to-Direct Band Gap Crossover in Few-Layer Transition Metal Dichalcogenides: A Theoretical Prediction. *J. Phys. Chem. C* **2016**, *120*, 21866.
(7) Pandey, S. K.; Das, R.; Mahadevan, P. Layer-Dependent Electronic Structure Changes in Transition Metal Dichalcogenides: The Microscopic Origin. *ACS Omega* **2020**, *5*, 15169.
(8) Ghatak, S.; Pal, A. N.; Ghosh, A. Nature of Electronic States in Atomically Thin MoS_2 Field-Effect Transistors. *ACS Nano* **2011**, *5*, 7707.
(9) Radisavljevic, B.; Radenovic, A.; Brivio, J.; Giacometti, V.; Kis, A. Single-Layer MoS_2 Transistors. *Nat. Nanotechnol.* **2011**, *6*, 147.
(10) Lembke, D.; Kis, A. Breakdown of High-Performance Monolayer MoS_2 Transistors. *ACS Nano* **2012**, *6*, 10070.
(11) Xu, X. D.; Yao, W.; Xiao, D.; Heinz, T. F. Spin and Pseudospins in Layered Transition Metal Dichalcogenides. *Nat. Phys.* **2014**, *10*, 343.
(12) Aivazian, G.; Gong, Z. R.; Jones, A. M.; Chu, R. L.; Yan, J.; Mandrus, D. G.; Zhang, C. W.; Cobden, D.; Yao, W.; Xu, X. Magnetic Control of Valley Pseudospin in Monolayer WSe_2. *Nat. Phys.* **2015**, *11*, 148.
(13) Ye, Z. L.; Sun, D. Z.; Heinz, T. F. Optical Manipulation of Valley Pseudospin. *Nat. Phys.* **2017**, *13*, 26.
(14) Li, J. X.; Li, W. Q.; Hung, S. H.; Chen, P. L.; Yang, Y. C.; Chang, T. Y.; Chiu, P. W.; Jeng, H. T.; Liu, C. H. Electric Control of Valley Polarization in Monolayer WSe_2 Using a van der Waals Magnet. *Nat. Nanotechnol.* **2022**, *17*, 721.
(15) Rocquefelte, X.; Boucher, F.; Gressier, P.; Ouvrard, G.; Blaha, P.; Schwarz, K. Mo Cluster Formation in the Intercalation Compound $LiMoS_2$. *Phys. Rev. B* **2000**, *62*, 2397.
(16) Rocquefelte, X.; Bouessay, I.; Boucher, F.; Gressier, P.; Ouvrard, G. Synergetic Theoretical and Experimental Structure Determination of Nanocrystalline Materials: Study of $LiMoS_2$. *J. Solid State Chem.* **2003**, *175*, 380.
(17) Petkov, V.; Billinge, S. J. L.; Larson, P.; Mahanti, S. D.; Vogt, T.; Rangan, K. K.; Kanatzidis, M. G. Structure of Nanocrystalline Materials Using Atomic Pair Distribution Function Analysis: Study of $LiMoS_2$. *Phys. Rev. B* **2002**, *65*, No. 092105.
(18) Fang, Y.; Pan, J.; Zhang, D.; Wang, D.; Hirose, H. T.; Terashima, T.; Uji, S.; Yuan, Y.; Li, W.; Tian, Z.; Xue, J.; Ma, Y.; Zhao, W.; Xue, Q.; Mu, G.; Zhang, H.; Huang, F. Discovery of Superconductivity in 2M WS_2 with Possible Topological Surface States. *Adv. Mater.* **2019**, *31*, No. 1901942.
(19) Fang, Y. Q.; Dong, Q.; Pan, J.; Liu, H. Y.; Liu, P.; Sun, Y. Y.; Li, Q. J.; Zhao, W.; Liu, B. B.; Huang, F. Q. Observation of Superconductivity in Pressurized 2M WSe_2 Crystals. *J. Mater. Chem. C* **2019**, *7*, 8551.
(20) Lai, Z. C.; He, Q. Y.; Ha Tran, T.; Repaka, D. V. M.; Zhou, D. D.; Sun, Y.; Xi, S. B.; Li, Y. X.; Chaturvedi, A.; Tan, C. L.; Chen, B.; Nam, G. H.; Li, B.; Ling, C. Y.; Zhai, W.; Shi, Z. Y.; Hu, D. Y.; Sharma, V.; Hu, Z. N.; Chen, Y.; Zhang, Z. C.; Yu, Y. F.; Wang, X. R.; Ramanujan, R. V.; Ma, Y. M.; Hippalgaonkar, K.; Zhang, H. Metastable 1T′-Phase Group VIB Transition Metal Dichalcogenide Crystals. *Nat. Mater.* **2021**, *20*, 1113.
(21) Dickinson, R. G.; Pauling, L. The Crystal Structure of Molybdenite. *J. Am. Chem. Soc.* **1923**, *45*, 1466.
(22) Schutte, W. J.; Deboer, J. L.; Jellinek, F. Crystal-Structures of Tungsten Disulfide and Diselenide. *J. Solid State Chem.* **1987**, *70*, 207.
(23) James, P. B.; Lavik, M. T. The Crystal Structure of $MoSe_2$. *Acta Crystallogr.* **1963**, *16*, 1183.
(24) Mahler, B.; Hoepfner, V.; Liao, K.; Ozin, G. A. Colloidal Synthesis of 1T-WS_2 and 2H-WS_2 Nanosheets: Applications for Photocatalytic Hydrogen Evolution. *J. Am. Chem. Soc.* **2014**, *136*, 14121.
(25) Sokolikova, M. S.; Sherrell, P. C.; Palczynski, P.; Bemmer, V. L.; Mattevi, C. Direct Solution-Phase Synthesis of 1T′ WSe2 Nanosheets. *Nat. Commun.* **2019**, *10*, No. 712.
(26) Geisenhoff, J. Q.; Tamura, A. K.; Schimpf, A. M. Using Ligands to Control Reactivity, Size and Phase in the Colloidal Synthesis of WSe_2 Nanocrystals. *Chem. Commun.* **2019**, *55*, 8856.
(27) Zhou, P. S.; Schiettecatte, P.; Vandichel, M.; Rousaki, A.; Vandenabeele, P.; Hens, Z.; Singh, S. Synthesis of Colloidal WSe_2 Nanocrystals: Polymorphism Control by Precursor-Ligand Chemistry. *Cryst. Growth Des.* **2021**, *21*, 1451.
(28) Liu, Z. Q.; Nie, K. K.; Qu, X. Y.; Li, X. H.; Li, B. J.; Yuan, Y. L.; Chong, S. K.; Liu, P.; Li, Y. G.; Yin, Z. Y.; Huang, W. General Bottom-Up Colloidal Synthesis of Nano-Monolayer Transition-Metal Dichalcogenides with High 1T′-Phase Purity. *J. Am. Chem. Soc.* **2022**, *144*, 4863.
(29) Kapuria, N.; Patil, N. N.; Sankaran, A.; Laffir, F.; Geaney, H.; Magner, E.; Scanlon, M.; Ryan, K. M.; Singh, S. Engineering Polymorphs in Colloidal Metal Dichalcogenides: Precursor-Mediated Phase Control, Molecular Insights Into Crystallisation Kinetics and Promising Electrochemical Activity. *J. Mater. Chem. A* **2023**, *11*, 11341.
(30) Brown, B. E. The Crystal Structures of WTe_2 and High-Temperature $MoTe_2$. *Acta Crystallogr.* **1966**, *20*, 268.
(31) Dawson, W. G.; Bullett, D. W. Electronic-Structure and Crystallography of $MoTe_2$ and WTe_2. *J. Phys. C Solid State* **1987**, *20*, 6159.
(32) Mentzen, B. F.; Sienko, M. J. Preparation and X-Ray Study of Mixed-Anion Tungsten Dichalcogenides. *Inorg. Chem.* **1976**, *15*, 2198.
(33) Qian, X. F.; Liu, J. W.; Fu, L.; Li, J. Quantum Spin Hall Effect in Two-Dimensional Transition Metal Dichalcogenides. *Science* **2014**, *346*, 1344.
(34) Ugeda, M. M.; Pulkin, A.; Tang, S. J.; Ryu, H.; Wu, Q. S.; Zhang, Y.; Wong, D.; Pedramrazi, Z.; Martin-Recio, A.; Chen, Y.; Wang, F.; Shen, Z. X.; Mo, S. K.; Yazyev, O. V.; Crommie, M. F. Observation of Topologically Protected States at Crystalline Phase Boundaries in Single-Layer WSe_2. *Nat. Commun.* **2018**, *9*, No. 3401.
(35) Li, Y. W.; Zheng, H. J.; Fang, Y. Q.; Zhang, D. Q.; Chen, Y. J.; Chen, C.; Liang, A. J.; Shi, W. J.; Pei, D.; Xu, L. X.; Liu, S.; Pan, J.; Lu, D. H.; Hashimoto, M.; Barinov, A.; Jung, S. W.; Cacho, C.; Wang, M. X.; He, Y.; Fu, L.; Zhang, H. J.; Huang, F. Q.; Yang, L. X.; Liu, Z. K.; Chen, Y. L. Observation of Topological Superconductivity in a Stoichiometric Transition Metal Dichalcogenide 2M-WS_2. *Nat. Commun.* **2021**, *12*, No. 2874.
(36) Lai, Z. C.; Yao, Y.; Li, S. Y.; Ma, L.; Zhang, Q. H.; Ge, Y. Y.; Zhai, W.; Chi, B. L.; Chen, B.; Li, L. J.; Wang, L.; Zheng, Z. J.; Gu, L.; Du, Y. H.; Zhang, H. Salt-Assisted 2H-to-1T′ Phase Transformation of Transition Metal Dichalcogenides. *Adv. Mater.* **2022**, *34*, No. 2201194.
(37) Dhakal, K. P.; Ghimire, G.; Chung, K.; Duong, D. L.; Kim, S. W.; Kim, J. Probing Multiphased Transition in Bulk MoS_2 by Direct Electron Injection. *ACS Nano* **2019**, *13*, 14437.
(38) Yin, X. M.; Wang, Q. X.; Cao, L.; Tang, C. S.; Luo, X.; Zheng, Y. J.; Wong, L. M.; Wang, S. J.; Quek, S. Y.; Zhang, W. J.; Rusydi, A.; Wee, A. T. S. Tunable Inverted Gap in Monolayer Quasi-Metallic MoS_2 Induced by Strong Charge-Lattice Coupling. *Nat. Commun.* **2017**, *8*, No. 486.
(39) Heising, J.; Kanatzidis, M. G. Exfoliated and Restacked MoS_2 and WS_2: Ionic or Neutral Species? Encapsulation and Ordering of Hard Electropositive Cations. *J. Am. Chem. Soc.* **1999**, *121*, 11720.
(40) Heising, J.; Kanatzidis, M. G. Structure of Restacked MoS_2 and WS_2 Elucidated by Electron Crystallography. *J. Am. Chem. Soc.* **1999**, *121*, 638.
(41) Petkov, V.; Billinge, S. J. L.; Heising, J.; Kanatzidis, M. G. Application of Atomic Pair Distribution Function Analysis to Materials with Intrinsic Disorder. Three-Dimensional Structure of Exfoliated-Restacked WS_2: Not Just a Random Turbostratic Assembly of Layers. *J. Am. Chem. Soc.* **2000**, *122*, 11571.
(42) Tan, S. J. R.; Abdelwahab, I.; Ding, Z.; Zhao, X.; Yang, T.; Loke, G. Z. J.; Lin, H.; Verzhbitskiy, I.; Poh, S. M.; Xu, H.; Nai, C. T.; Zhou, W.; Eda, G.; Jia, B.; Loh, K. P. Chemical Stabilization of 1T′ Phase Transition Metal Dichalcogenides with Giant Optical Kerr Nonlinearity. *J. Am. Chem. Soc.* **2017**, *139*, 2504.
(43) Sun, L. F.; Yan, X. X.; Zheng, J. Y.; Yu, H. D.; Lu, Z. X.; Gao, S. P.; Liu, L. N.; Pan, X. Q.; Wang, D.; Wang, Z. G.; Wang, P.; Jiao, L. Y.

https://doi.org/10.1021/acs.chemmater.4c01602
Chem. Mater. 2024, 36, 8834−8845

Layer-Dependent Chemically Induced Phase Transition of Two-Dimensional MoS_2. *Nano Lett.* **2018**, *18*, 3435.
(44) Leng, K.; Chen, Z. X.; Zhao, X. X.; Tang, W.; Tian, B. B.; Nai, C. T.; Zhou, W.; Loh, K. P. Phase Restructuring in Transition Metal Dichalcogenides for Highly Stable Energy Storage. *ACS Nano* **2016**, *10*, 9208.
(45) Xia, J.; Wang, J.; Chao, D. L.; Chen, Z.; Liu, Z.; Kuo, J. L.; Yan, J. X.; Shen, Z. X. Phase Evolution of Lithium Intercalation Dynamics in 2H-MoS_2. *Nanoscale* **2017**, *9*, 7533.
(46) Cho, S.; Kim, S.; Kim, J. H.; Zhao, J.; Seok, J.; Keum, D. H.; Baik, J.; Choe, D. H.; Chang, K. J.; Suenaga, K.; Kim, S. W.; Lee, Y. H.; Yang, H. Phase Patterning for Ohmic Homojunction Contact in $MoTe_2$. *Science* **2015**, *349*, 625.
(47) Zhu, J. Q.; Wang, Z. C.; Yu, H.; Li, N.; Zhang, J.; Meng, J. L.; Liao, M. Z.; Zhao, J.; Lu, X. B.; Du, L. J.; Yang, R.; Shi, D.; Jiang, Y.; Zhang, G. Y. Argon Plasma Induced Phase Transition in Monolayer MoS_2. *J. Am. Chem. Soc.* **2017**, *139*, 10216.
(48) Song, S.; Keum, D. H.; Cho, S.; Perello, D.; Kim, Y.; Lee, Y. H. Room Temperature Semiconductor−Metal Transition of $MoTe_2$ Thin Films Engineered by Strain. *Nano Lett.* **2016**, *16*, 188.
(49) Tong, X.; Qi, Y. H.; Chen, J.; Wang, N.; Xu, Q. Supercritical CO_2-Assisted Reverse-Micelle-Induced Solution-Phase Fabrication of Two-Dimensional Metallic 1T-MoS_2 and 1T-WS_2. *Chemnanomat* **2017**, *3*, 466.
(50) Song, X.; Hoff, B.; Singha, R.; Stiles, J. W.; Skorupskii, G.; Khoury, J. F.; Cheng, G.; Kamm, F.; Uzan, A. J.; Dulovic, S.; Wu, S.; Pielnhofer, F.; Yao, N.; Schoop, L. M. Acid-Assisted Soft Chemical Route for Preparing High-Quality Superconducting 2M-WS_2. *Chem. Mater.* **2023**, *35*, 5487.
(51) Pan, D. C.; An, L. J.; Sun, Z. M.; Hou, W.; Yang, Y.; Yang, Z. Z.; Lu, Y. F. Synthesis of Cu−In−S Ternary Nanocrystals with Tunable Structure and Composition. *J. Am. Chem. Soc.* **2008**, *130*, 5620.
(52) Guo, Q.; Kim, S. J.; Kar, M.; Shafarman, W. N.; Birkmire, R. W.; Stach, E. A.; Agrawal, R.; Hillhouse, H. W. Development of $CuInSe_2$ Nanocrystal and Nanoring Inks for Low-Cost Solar Cells. *Nano Lett.* **2008**, *8*, 2982.
(53) Norako, M. E.; Brutchey, R. L. Synthesis of Metastable Wurtzite $CuInSe_2$ Nanocrystals. *Chem. Mater.* **2010**, *22*, 1613.
(54) Rhodes, J. M.; Jones, C. A.; Thal, L. B.; Macdonald, J. E. Phase-Controlled Colloidal Syntheses of Iron Sulfide Nanocrystals via Sulfur Precursor Reactivity and Direct Pyrite Precipitation. *Chem. Mater.* **2017**, *29*, 8521.
(55) Tappan, B. A.; Barim, G.; Kwok, J. C.; Brutchey, R. L. Utilizing Diselenide Precursors toward Rationally Controlled Synthesis of Metastable $CuInSe_2$ Nanocrystals. *Chem. Mater.* **2018**, *30*, 5704.
(56) Barim, G.; Smock, S. R.; Antunez, P. D.; Glaser, D.; Brutchey, R. L. Phase Control in the Colloidal Synthesis of Well-Defined Nickel Sulfide Nanocrystals. *Nanoscale* **2018**, *10*, 16298.
(57) Tappan, B. A.; Horton, M. K.; Brutchey, R. L. Ligand-Mediated Phase Control in Colloidal $AgInSe_2$ Nanocrystals. *Chem. Mater.* **2020**, *32*, 2935.
(58) Tappan, B. A.; Brutchey, R. L. Polymorphic Metastability in Colloidal Semiconductor Nanocrystals. *Chemnanomat* **2020**, *6*, 1567.
(59) Robinson, E. H.; Dwyer, K. M.; Koziel, A. C.; Nuriye, A. Y.; Macdonald, J. E. Synthesis of Vulcanite (CuTe) and Metastable $Cu_{1.5}Te$ Nanocrystals Using a Dialkyl Ditelluride Precursor. *Nanoscale* **2020**, *12*, 23036.
(60) Lord, R. W.; Fanghanel, J.; Holder, C. F.; Dabo, I.; Schaak, R. E. Colloidal Nanoparticles of a Metastable Copper Selenide Phase with Near-Infrared Plasmon Resonance. *Chem. Mater.* **2020**, *32*, 10227.
(61) Ho, E. A.; Peng, A. R.; Macdonald, J. E. Alkyl Selenol Reactivity With Common Solvents and Ligands: Influences on Phase Control in Nanocrystal Synthesis. *Nanoscale* **2021**, *14*, 76.
(62) Lee, S. H.; Hoyer, C. E.; Liao, C.; Li, X. S.; Holmberg, V. C. Phase-Controlled Synthesis and Quasi-Static Dielectric Resonances in Silver Iron Sulfide ($AgFeS_2$) Nanocrystals. *Small* **2022**, *18*, No. 2104975.
(63) Geisenhoff, J. Q.; Yin, H.; Oget, N.; Chang, H.; Chen, L.; Schimpf, A. M. Controlled CO Labilization of Tungsten Carbonyl Precursors for the Low-Temperature Synthesis of Tungsten Diselenide Nanocrystals. *Front. Nanotechnol.* **2022**, *4*, No. 1026635.
(64) Niebur, A.; Söll, A.; Haizmann, P.; Strolka, O.; Rudolph, D.; Tran, K.; Renz, F.; Frauendorf, A. P.; Hübner, J.; Peisert, H.; Scheele, M.; Lauth, J. Untangling the Intertwined: Metallic to Semiconducting Phase Transition of Colloidal MoS_2 Nanoplatelets and Nanosheets. *Nanoscale* **2023**, *15*, 5679.
(65) Shults, A. A.; Lu, G. Y.; Caldwell, J. D.; Macdonald, J. E. Role of Carboxylates in the Phase Determination of Metal Sulfide Nanoparticles. *Nanoscale Horiz.* **2023**, *8*, 1386.
(66) Gendler, D.; Bi, J. Y.; Mekan, D.; Warokomski, A.; Armstrong, C.; Hernandez-Pagan, E. A. Halide-Driven Polymorph Selectivity in the Synthesis of MnX (X = S, Se) Nanoparticles. *Nanoscale* **2023**, *15*, 2650.
(67) Endres, E. J.; Espano, J. R. B.; Koziel, A.; Peng, A. R.; Shults, A. A.; Macdonald, J. E. Controlling Phase in Colloidal Synthesis. *ACS Nanosci. Au* **2024**, *4*, 158.
(68) Kwon, I. S.; Kwak, I. H.; Kim, J. Y.; Lee, S. J.; Sial, Q. A.; Ihsan, J.; Lee, K. S.; Yoo, S. J.; Park, J.; Kang, H. S. 2H−2M Phase Control of WSe_2 Nanosheets by Se Enrichment Toward Enhanced Electrocatalytic Hydrogen Evolution Reaction. *Adv. Mater.* **2023**, *36*, No. 2307867.
(69) Wang, Y. W.; He, J. T.; Liu, C. C.; Chong, W. H.; Chen, H. Y. Thermodynamics Versus Kinetics in Nanosynthesis. *Angew. Chem., Int. Ed.* **2015**, *54*, 2022.
(70) Martinolich, A. J.; Neilson, J. R. Toward Reaction-by-Design: Achieving Kinetic Control of Solid State Chemistry with Metathesis. *Chem. Mater.* **2017**, *29*, 479.
(71) Kanatzidis, M. G.; Poeppelmeier, K. R.; et al. Report from the Third Workshop on Future Directions of Solid-State Chemistry: The Status of Solid-State Chemistry and Its Impact in the Physical Sciences. *Prog. Solid State Chem.* **2008**, *36*, 1.
(72) Ostwald, W. Studien über die Bildung und Umwandlung fester Körper: 1. Abhandlung: Übersättigung und Überkaltung. *Z. Phys. Chem.* **1897**, *22U*, 289.
(73) Rein ten Wolde, P.; Frenkel, D. Homogeneous Nucleation and the Ostwald Step Rule. *Phys. Chem. Chem. Phys.* **1999**, *1*, 2191.
(74) Cardew, P. T.; Davey, R. J. The Ostwald Ratio, Kinetic Phase Diagrams, and Polymorph Maps. *Cryst. Growth Des.* **2019**, *19*, 5798.
(75) Andrews, J. L.; Pearson, E.; Yufit, D. S.; Steed, J. W.; Edkins, K. Supramolecular Gelation as the First Stage in Ostwald's Rule. *Cryst. Growth Des.* **2018**, *18*, 7690.
(76) Cheetham, A. K.; Kieslich, G.; Yeung, H. H.-M. Thermodynamic and Kinetic Effects in the Crystallization of Metal−Organic Frameworks. *Acc. Chem. Res.* **2018**, *51*, 659.
(77) Liu, Z. Q.; Li, N.; Su, C.; Zhao, H. Y.; Xu, L. L.; Yin, Z. Y.; Li, J.; Du, Y. P. Colloidal synthesis of 1T′ Phase Dominated WS_2 Towards Endurable Electrocatalysis. *Nano Energy* **2018**, *50*, 176.
(78) Geisenhoff, J. Q.; Tamura, A. K.; Schimpf, A. M. Manipulation of Precursor Reactivity for the Facile Synthesis of Heterostructured and Hollow Metal Selenide Nanocrystals. *Chem. Mater.* **2020**, *32*, 2304.
(79) Sokolikova, M. S.; Cheng, G.; Och, M.; Palczynski, P.; El Hajraoui, K.; Ramasse, Q. M.; Mattevi, C. Tuning the 1T′/2H Phases in $W_xMo_{1-x}Se_2$ Nanosheets. *Nanoscale* **2023**, *15*, 2714.
(80) Duerloo, K. A. N.; Li, Y.; Reed, E. J. Structural Phase Transitions in Two-Dimensional Mo- and W-Dichalcogenide Monolayers. *Nat. Commun.* **2014**, *5*, No. 4214.
(81) Shahmanesh, A.; Romanin, D.; Dabard, C.; Chee, S.-S.; Gréboval, C.; Methivier, C.; Silly, M. G.; Chaste, J.; Bugnet, M.; Pierucci, D.; Ouerghi, A.; Calandra, M.; Lhuillier, E.; Mahler, B. 2D Monolayer of the 1T′ Phase of Alloyed WSSe from Colloidal Synthesis. *J. Phys. Chem. C* **2021**, *125*, 11058.
(82) Jiang, M.; Zhang, J. J.; Wu, M. H.; Jian, W. J.; Xue, H. T.; Ng, T.-W.; Lee, C. S.; Xu, J. Synthesis of 1T-$MoSe_2$ Ultrathin Nanosheets with an Expanded Interlayer Spacing of 1.17 nm for Efficient Hydrogen Evolution Reaction. *J. Mater. Chem. A* **2016**, *4*, 14949.

https://doi.org/10.1021/acs.chemmater.4c01602
Chem. Mater. 2024, 36, 8834−8845

(83) Scarfiello, R.; Cesari, A.; Altamura, D.; Masi, S.; Nobile, C.; Balzano, F.; Giannini, C.; Grillo, V.; Tavabi, A. H.; Dunin-Borkowski, R. E.; Uccello-Barretta, G.; Cozzoli, P. D.; Rizzo, A. Mechanistic Insight into the Formation of Colloidal WS_2 Nanoflakes in Hot Alkylamine Media. *Nanoscale Adv.* **2019**, *1*, 2772.
(84) Pippia, G.; Van Hamme, D.; Martin-Garcia, B.; Prato, M.; Moreels, I. A Colloidal Route to Semiconducting Tungsten Disulfide Nanosheets with Monolayer Thickness. *Nanoscale* **2022**, *14*, 15859.
(85) Kwon, I. S.; Kwak, I. H.; Debela, T. T.; Kim, J. Y.; Yoo, S. J.; Kim, J.-G.; Park, J.; Kang, H. S. Phase-Transition $Mo_{1-x}VxSe_2$ Alloy Nanosheets with Rich V−Se Vacancies and Their Enhanced Catalytic Performance of Hydrogen Evolution Reaction. *ACS Nano* **2021**, *15*, 14672.
(86) Kwak, I. H.; Kwon, I. S.; Debela, T. T.; Abbas, H. G.; Park, Y. C.; Seo, J.; Ahn, J. P.; Lee, J. H.; Park, J.; Kang, H. S. Phase Evolution of $Re_{1-x}Mo_xSe_2$ Alloy Nanosheets and Their Enhanced Catalytic Activity toward Hydrogen Evolution Reaction. *ACS Nano* **2020**, *14*, 11995.
(87) Hall, B. D. Debye Function Analysis of Structure in Diffraction From Nanometer-Sized Particles. *J. Appl. Phys.* **2000**, *87*, 1666.
(88) Mead, D. G.; Irwin, J. C. Long Wavelength Optic Phonons in WSe_2. *Can. J. Phys.* **1977**, *55*, 379.
(89) Zhao, W. J.; Ghorannevis, Z.; Amara, K. K.; Pang, J. R.; Toh, M.; Zhang, X.; Kloc, C.; Tan, P. H.; Eda, G. Lattice Dynamics in Mono- and Few-Layer Sheets of WS_2 and WSe_2. *Nanoscale* **2013**, *5*, 9677.
(90) del Corro, E.; Terrones, H.; Elias, A.; Fantini, C.; Feng, S. M.; Nguyen, M. A.; Mallouk, T. E.; Terrones, M.; Pimenta, M. A. Excited Excitonic States in 1L, 2L, 3L, and Bulk WSe_2 Observed by Resonant Raman Spectroscopy. *ACS Nano* **2014**, *8*, 9629.
(91) Cheng, F.; Hu, Z. X.; Xu, H.; Shao, Y.; Su, J.; Chen, Z.; Ji, W.; Loh, K. P. Interface Engineering of Au(111) for the Growth of 1T′-$MoSe_2$. *ACS Nano* **2019**, *13*, 2316.
(92) Xu, J. G.; Ho, D. R. Modulation of the Reaction Mechanism via S/Mo: A Rational Strategy for Large-Area MoS_2 Growth. *Chem. Mater.* **2021**, *33*, 3249.
(93) Wang, D.; Zhang, Z. W.; Huang, B. L.; Zhang, H. M.; Huang, Z. W.; Liu, M. M.; Duan, X. D. Few-Layer WS_2−WSe_2 Lateral Heterostructures: Influence of the Gas Precursor Selenium/Tungsten Ratio on the Number of Layers. *ACS Nano* **2022**, *16*, 1198.
(94) Kwon, I. S.; Kwak, I. H.; Debela, T. T.; Abbas, H. G.; Park, Y. C.; Ahn, J.-P.; Park, J.; Kang, H. S. Se-Rich $MoSe_2$ Nanosheets and Their Superior Electrocatalytic Performance for Hydrogen Evolution Reaction. *ACS Nano* **2020**, *14*, 6295.
(95) Lei, T.; Gu, M. Y.; Fu, H. W.; Wang, J.; Wang, L. L.; Zhou, J.; Liu, H.; Lu, B. A. Bond Modulation of $MoSe_{2+x}$ Driving Combined Intercalation and Conversion Reactions for High-Performance K Cathodes. *Chem. Sci.* **2023**, *14*, 2528.
(96) Erk, C.; Rohner, C.; Schlecht, S. Formation of Crystalline CdSe Particles from a Single-Source-Precursor According to Ostwald's Rule. *Z. Anorg. Allg. Chem.* **2008**, *634*, 3001.
(97) Washington, A. L.; Foley, M. E.; Cheong, S.; Quffa, L.; Breshike, C. J.; Watt, J.; Tilley, R. D.; Strouse, G. F. Ostwald's Rule of Stages and Its Role in CdSe Quantum Dot Crystallization. *J. Am. Chem. Soc.* **2012**, *134*, 17046.
(98) Sato, K. Polymorphic Transformations in Crystal-Growth. *J. Phys. D Appl. Phys.* **1993**, *26*, B77.
(99) Cardew, P. T.; Davey, R. J. The Kinetics of Solvent-Mediated Phase-Transformations. *Proc. R. Soc. London, Ser. A* **1985**, *398*, 415.
(100) Cardew, P. T.; Davey, R. J.; Ruddick, A. J. Kinetics of Polymorphic Solid-State Transformations. *J. Chem. Soc., Faraday Trans. 2* **1984**, *80*, 659.
(101) Fang, Z.; Li, X.; Shi, W. H.; Li, Z. W.; Guo, Y. F.; Chen, Q.; Peng, L. M.; Wei, X. L. Interlayer Binding Energy of Hexagonal MoS_2 as Determined by an In Situ Peeling-to-Fracture Method. *J. Phys. Chem. C* **2020**, *124*, 23419.
(102) Liu, X. Y.; Zhang, P. T.; Wang, S. Y.; Fang, Y. Q.; Wu, P. H.; Xiang, Y.; Chen, J. P.; Zhao, C. D.; Zhang, X.; Zhao, W.; Wang, J. J.; Huang, F. Q.; Guan, C. High Intrinsic Phase Stability of Ultrathin 2M WS_2. *Nat. Commun.* **2024**, *15*, No. 1263.
(103) Kresse, G.; Furthmuller, J. Efficiency of Ab-Initio Total Energy Calculations for Metals and Semiconductors Using a Plane-Wave Basis Set. *Comput. Mater. Sci.* **1996**, *6*, 15.
(104) Perdew, J. P.; Burke, K.; Ernzerhof, M. Generalized Gradient Approximation Made Simple. *Phys. Rev. Lett.* **1996**, *77*, 3865.
(105) Langreth, D. C.; Mehl, M. J. Beyond the Local-Density Approximation in Calculations of Ground-State Electronic-Properties. *Phys. Rev. B* **1983**, *28*, 1809.
(106) Becke, A. D. Density-Functional Exchange-Energy Approximation with Correct Asymptotic-Behavior. *Phys. Rev. A* **1988**, *38*, 3098.
(107) Blöchl, P. E. Projector Augmented-Wave Method. *Phys. Rev. B* **1994**, *50*, 17953.
(108) Johnson, E. R.; Becke, A. D. A Post-Hartree−Fock Model of Intermolecular Interactions: Inclusion of Higher-Order Corrections. *J. Chem. Phys.* **2006**, *124*, No. 174104.
(109) Grimme, S.; Antony, J.; Ehrlich, S.; Krieg, H. A Consistent and Accurate Ab Initio Parametrization of Density Functional Dispersion Correction (DFT-D) For the 94 Elements H−Pu. *J. Chem. Phys.* **2010**, *132*, No. 154104.
(110) Grimme, S.; Ehrlich, S.; Goerigk, L. Effect of the Damping Function in Dispersion Corrected Density Functional Theory. *J. Comput. Chem.* **2011**, *32*, 1456.

https://doi.org/10.1021/acs.chemmater.4c01602
Chem. Mater. 2024, 36, 8834−8845